Superfluid rings as quantum pendulums

Antonio Muñoz Mateo ⬤

Departamento de Física, Universidad de La Laguna, 38200 Tenerife, Spain

Grigory E. Astrakharchik ⬤

Departament de Física, Universitat Politècnica de Catalunya, 08034 Barcelona, Spain;
Departament de Física Quàntica i Astrofísica, Universitat de Barcelona, Martí Franquès 1, 08028 Barcelona, Spain;
and Institut de Ciències del Cosmos (ICCUB), Universitat de Barcelona, Martí Franquès, 1, 08028 Barcelona, Spain

Bruno Juliá-Díaz ⬤

Departament de Física Quàntica i Astrofísica, Universitat de Barcelona, Martí Franquès 1, 08028 Barcelona, Spain
and Institut de Ciències del Cosmos (ICCUB), Universitat de Barcelona, Martí Franquès, 1, 08028 Barcelona, Spain

A nondispersive quantum pendulum is presented. The proposed setup consists of an ultracold atomic cloud, featuring attractive interatomic interactions, loaded into a tilted ring potential. The classical and quantum domains are switched on by tuned interactions, and the classical dynamical stabilization of unstable states, i.e., à la Kapitza, is shown to be driven by quantum phase imprinting. One potential application of this system as a gravimeter is discussed.

I. INTRODUCTION

Ring geometries are omnipresent in physics. Mathematically, they endow systems with periodic boundary conditions; physically, they realize the minimal block of cyclic transport, which would become perpetual if there were no dissipation. Approaching the dissipationless limit, superconductors and superfluids are capable of making the cyclic transport of charge or particles, if not perpetual, at least persistent, a particularly striking demonstration of which is the persistent flow of superconducting gravimeters [1]. In this regard, the first realizations of ring geometries in ultracold gases opened new avenues for experiments with persistent currents of highly controlled Bose-Einstein condensates [2–5]. However, in this case, the gravitational pull is an apparent hindrance to stationary flows, since a small tilting of the ring axis with respect to the vertical direction gives rise to an unwanted azimuthal potential for the trapped atoms [3,6]. Interestingly, although suppression of the tilting is necessary for the study of unobstructed currents, by letting the tilting occur, the ring is transformed into a pendulum (see Fig. 1); for instance, horizontally setting the axis of a typical ring of radius $R = 20\,\mu\mathrm{m}$ converts it into a pendulum of angular frequency $\omega = \sqrt{g/R} = 700\,\mathrm{rad/s}$, where g is the gravity acceleration. While for a repulsively interacting, extended Bose-Einstein condensate (BEC) the resemblance to the classical pendulum would only apply to the motion of the center of mass, one expects to find its quantum analog in attractively interacting, localized BECs. The present work is devoted to exploring the validity of this analogy. Among potential applications, we discuss the basic features of a gravimeter based on the quantum pendulum.

The pendulum dynamics has been addressed under multiple perspectives in the context of ultracold atomic systems. Its presence is implicitly evident in the coherent tunneling of particles, as observed in the Josephson effect [7–9]. Additionally, the proposal for the dynamic generation of nonlinear excitations has shed further light on the intricacies of pendulum dynamics in this context [10]. Most of the studies have focused on the dynamical stabilization of pendulum-like equilibrium states in optical potentials that are unstable [11–13]. Closer to our discussion on dynamical stabilization, Ref. [14] addressed the general dynamics of bright solitons in periodically, rapidly varying time traps. In a classical context, the pendulum dynamics of a microscopic colloidal particle in a ring built with optical tweezers has been recently reported [15].

II. THE TILTED RING

We assume a quasi-one-dimensional character of the system, which can be ensured by imposing tight transverse confinement to the atoms. While the role of quantum fluctuations is enhanced in one dimension, still, in the mean-field regime, the gas is sufficiently coherent to be correctly described by the Gross-Pitaevskii equation [Eq. (1) below]. Although strictly speaking Bose-Einstein condensation is absent in one dimension, properties of a quasicondensate are
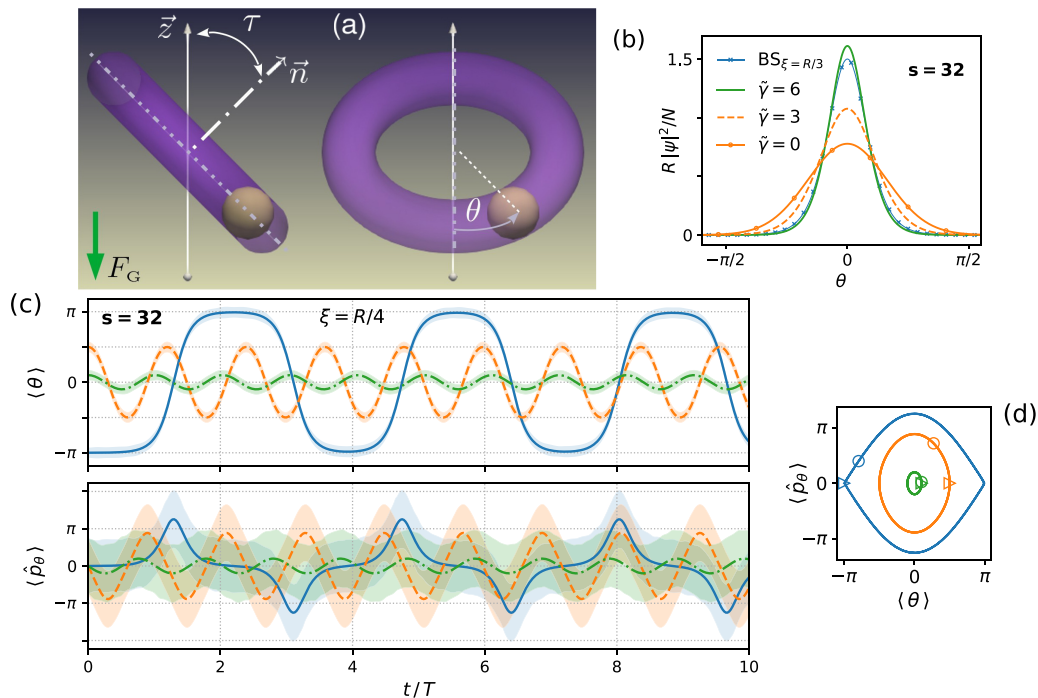
FIG. 1. (a) Schematic picture, side (left) and front (right) views, of a tilted ring potential (purple isocontour) inside which a BEC (cream blob) moves in the presence of the constant gravitational force F_G. (b) Ground-state density profile in a ring trap, characterized by the angular frequency $\omega = 2\hbar/mR^2$ and potential depth $s = 32$ (see text), for various strengths of the interparticle attraction, parametrized by $\tilde{\gamma} = |\gamma|mNR/\hbar^2$. (c) Oscillations of the center of mass (top panel) and the average momentum (bottom panel) of a bright soliton of width $\xi = R/4$ (or, equivalently, $\tilde{\gamma} = 8$) for different initial positions. The shaded areas around the solid lines represent the mean width in position σ and momentum σ_k spaces. (d) Trajectories in the phase space. States at $t = 0$ (triangles) and $t = T$ (circles) are indicated by open symbols.

correctly captured by equations describing the evolution of the condensate wave function. A tilting angle $\tau \in [0, \pi/2]$ produces on the particles of mass m the gravitational potential $U(\tau, \theta) = -mgR \sin\tau \cos\theta$ along the azimuthal coordinate $\theta \in [-\pi, \pi]$ of the ring, or alternatively, $U(\tau, \theta) = -m\omega^2 R^2 \cos\theta$, where $\omega = \sqrt{g\sin\tau/R}$ is the pendulum angular frequency, so $T = 2\pi/\omega$ is the corresponding time period, see the depiction in Fig. 1. For noninteracting particles, the time evolution is described by the Schrödinger equation, i.e., Eq. (1) with $\gamma = 0$ (see the early discussion of pendulums in quantum mechanics by Condon [16], or for a more recent account, for instance, Ref. [17]). It admits general solutions that can be written as superpositions of Mathieu functions [18] $ce_{2n}(\theta, q)$ and $se_{2n+1}(\theta, q)$, with $n = 0, 1, 2, \ldots$, and $2q = -(2R/a_{ho})^4$. Here, we have introduced the harmonic oscillator length, $a_{ho} = \sqrt{\hbar/m\omega}$, associated with small-amplitude oscillations around the equilibrium point $\theta = 0$. For $q \to 0$, that is, for a small tilting or $\omega \to 0$, these functions tend to the trigonometric functions $\cos(2n\theta)$ and $\sin[(2n+1)\theta]$.

Deeper insights can be drawn by considering the particle positions along the circumference of the ring. The potential felt by a particle located at position x can be expressed by substituting the azimuthal angle by $\theta = 2\pi x/d$, where $d = 2\pi R$ is the circumference of the ring, leading to $U(\tau, x) = -gmR \sin\tau + 2gmR \sin\tau \sin^2(\pi x/d)$. The resulting tilting potential can be conceptualized [19] as a periodic lattice potential $V_0 \sin^2(\pi x/d)$ of amplitude $V_0 = 2gmR \sin\tau = 2m\omega^2 R^2$. In this context, the natural energy scale in a lattice is given by $E_L = \hbar^2\pi^2/(2md^2) = \hbar^2/(8mR^2)$, referred

to as the *recoil energy* [20]. The dimensionless ratio between lattice amplitude and the recoil energy, denoted as $s = (1/2) V_0/E_L = 8m^2\omega^2 R^4/\hbar^2$ (with an extra $1/2$ factor as compared to the usual convention [21]), quantifies the lattice depth and matches in absolute value the Mathieu-function parameter $s = |q|$. A shallow lattice is characterized by $s \lesssim 1$, while a deep lattice corresponds to $s \gg 1$. As in the tilted ring only a single lattice site is available, i.e., $0 \leqslant x \leqslant d$, the ring displays a minimal band structure composed of a single Bloch state, with zero quasimomentum, per energy band [22]. In Fig. 2(a) two opposite limits are shown, corresponding to shallow ($s = 0.5$) and deep ($s = 32$) lattices. The three lowest-energy eigenstates $\psi_{n,0}$ are shown with $n = 0, 1, 2, \ldots$, standing for the band index and reflecting the number of nodes. As expected, the density becomes increasingly localized as the lattice amplitude is augmented. In the limit of very large s, the lowest eigenstates are similar to those of a harmonic oscillator.

For the interacting gas, the system dynamics obeys the time-dependent Gross-Pitaevskii equation

$$i\hbar\partial_t\psi = \left(-\frac{\hbar^2}{2mR^2}\partial_\theta^2 - m\omega^2 R^2 \cos\theta + \gamma|\psi|^2\right)\psi, \quad (1)$$

where $\gamma = -2\hbar^2/(ma_{1D}) < 0$ denotes the coupling constant of the attractive interparticle interaction and a_{1D} is the s-wave scattering length [23]. The number of particles fixes the wave function normalization $N = R \int d\theta |\psi|^2$, while the energy E is provided by the functional
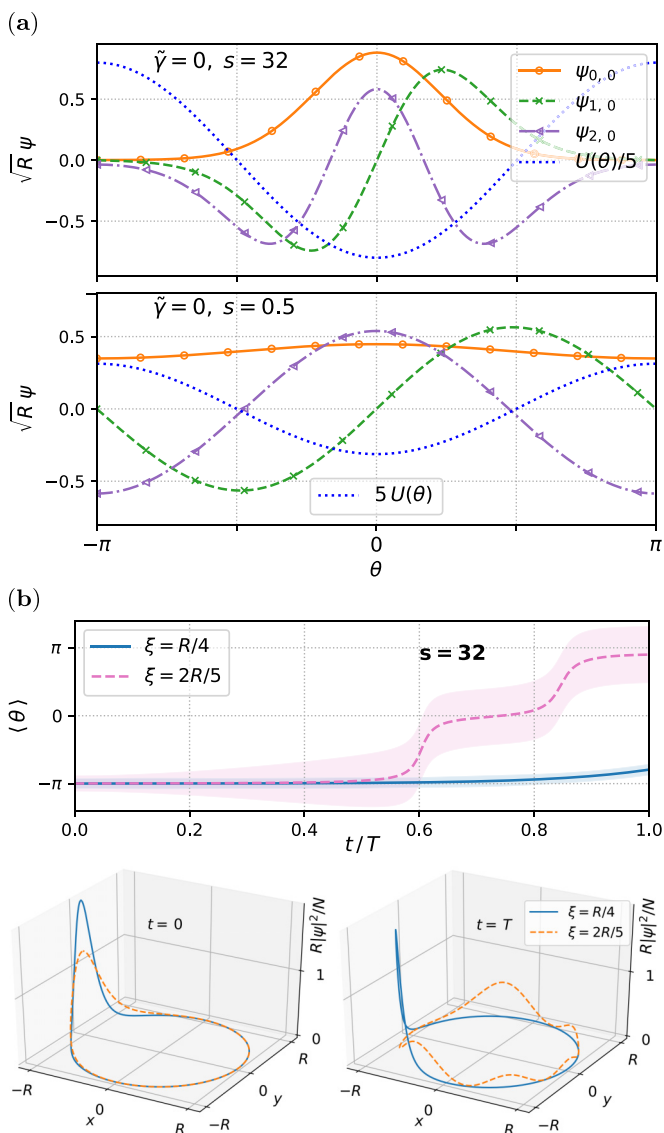
FIG. 2. (a) Lowest-energy eigenstates (Mathieu functions) of noninteracting systems with potential depths $s = 32$ (top panel) and $s = 0.5$ (bottom panel). (b) Dynamics dependence on the width ξ of an initial wave packet (a free soliton) centered close to the classical unstable equilibrium point $\theta = \pi$ [in Cartesian coordinates $(x, y) = (-R, 0)$]. The top panel shows the time evolution of the center of mass for $\xi = R/4$ (or interaction parameter $\tilde{\gamma} = 8$) and $\xi = 2R/5$ ($\tilde{\gamma} = 5$). While the former case, well beyond the threshold width for the existence of equilibrium states at $\theta = \pi$, follows the classical path (the same shown in Fig. 1 for much longer evolution), the wider soliton spreads over the ring (bottom panels).

$E[\psi] = R \int d\theta (\hbar^2 |\partial_\theta \psi|^2 / 2mR^2 - m\omega^2 R^2 \cos\theta |\psi|^2 + \gamma |\psi|^4 / 2)$. Expectation values are computed as quantum-mechanical averages, $\langle A \rangle = (1/N)R \int d\theta \, \psi^* A \psi$, where the $1/N$ appears due to the wave function normalization. Figure 1(b) illustrates the effect of increasing attractive interactions on the ground-state density profile, which becomes increasingly localized. When the interparticle interaction dominates over the external potential, the ground state approaches a free

bright soliton centered at $\theta_0 = 0$,

$$\psi_{BS}(\theta) = \sqrt{\frac{N}{2\xi}} \, \text{sech}\left(R\frac{\theta - \theta_0}{\xi} \right), \qquad (2)$$

whose width $\xi = 2\hbar^2/(m|\gamma|N) = a_{1D}/N$ scales inversely with the number of particles, while the peak density does so quadratically.

The close analogy between this system and the classical pendulum is evidenced by the time evolution of expectation values, as obtained from the Ehrenfest equations (see Appendix A). An illustrative example is represented in Fig. 1(c), where the evolution of the center of mass $\langle\theta\rangle$ and the angular momentum $\langle\hat{p}_\theta\rangle$ is shown for a soliton of width $\xi = R/4$ in a deep lattice with $s = 32$. The time evolution follows the equations of motion $mR^2 d\langle\theta\rangle/dt = \langle\hat{p}_\theta\rangle$ and $d\langle\hat{p}_\theta\rangle/dt = -\langle\partial_\theta U\rangle$ and, in agreement with Kohn's theorem, is independent of the interaction strength. Hence, the nonlinear equation of the pendulum is $d^2\langle\theta\rangle/dt^2 + \omega^2\langle\sin\theta\rangle = 0$. Nevertheless, the analogy with the classical system is not always fulfilled. Had we chosen a wider wave packet (say $\xi = 2R/5$) centered at the potential maximum as the initial state, it would spread over the ring, since the wave packet falls onto both sides of the maximum, as illustrated in Fig. 2(b). We show next that this observation reflects the lack of the classical equilibrium point at $\theta_0 = \pi$, whose existence depends on the system parameters.

III. NONLINEAR SPECTRUM

The lattice viewpoint offers valuable insight into the structure of the spectrum of the nonlinear system. By switching on the interaction, the linear Bloch states [22] characterized by a given quasimomentum extend into the nonlinear regime while maintaining the number of nodes, which stands as a distinctive topological feature. In addition, nonlinear lattice systems allow for new stationary states of different nature, namely, the *gap solitons*. Contrary to Bloch waves in an infinite lattice, which are extended states over the whole system, gap solitons are localized states that occupy a few lattice sites (see Ref. [21], and references therein). In static systems, such states emerge within the energy gaps of the underlying linear system beyond an interaction threshold [19,24]. In the tilted ring, gap solitons emerge as states centered at the potential maximum.

Figure 3 illustrates the characteristic differences in the spectrum between shallow ($s = 0.5$) and deep ($s = 32$) lattices. The chemical potential is reported as a function of the interaction strength. The states labeled by $\psi_{n,0}$ represent the nonlinear continuation of the linear solutions shown in Fig. 2. These states have the center of mass located at the potential minimum $\theta = 0$. Beyond a certain interaction threshold, a new nonlinear state emerges (shown by the continuous line with symbols and labeled as $\psi_{0,\pi}$) with location at the potential maximum. Thus, these states are centered in the classically unstable equilibrium position of the inverted pendulum with $\theta = \pi$.

The emergence of equilibrium states at the potential maximum can be understood by expanding the potential around $\theta = \pi$, up to second order in the position. This results in a expulsive harmonic potential $U(\pi + \delta\theta) -$
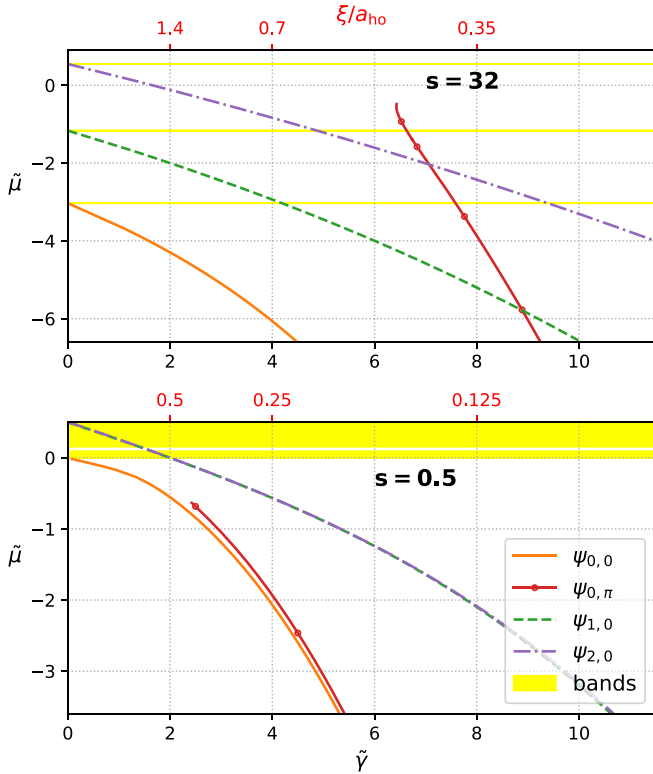
FIG. 3. Chemical potential of stationary states $\tilde{\mu} = \mu/(\hbar^2/mR^2)$ vs interaction strength $\tilde{\gamma} = |\gamma|mNR/\hbar^2$, for deep potential $s = 32$ (top panel) and shallow potential $s = 0.5$ (bottom panel). The linear energy bands of an infinite lattice with the same spacing (yellow shaded regions) are shown as a reference. The top horizontal axis of each graph indicates the width of a free soliton ξ in units of the harmonic oscillator length $a_{\rm ho}$.

$U(\pi) \approx -m\omega^2 R^2 \delta\theta^2/2$. Here, the soliton Eq. (2) centered in $\theta_0 = \pi$, with the soliton width ξ as a variational parameter, provides an ansatz. The energy in this system is given by the standard Gross-Pitaevskii energy functional (see, for example, Ref. [25] for details). By performing the energy minimization we arrive at the following quartic equation $1 - (a_{\rm ho}/\xi_f)\xi/a_{\rm ho} + (\pi/4)(\xi/a_{\rm ho})^4 = 0$, where $\xi_f = 2\hbar^2/(m|\gamma|N)$ is the free soliton width. This expression is valid when both $\xi \ll R$ and $\xi_f \ll R$. For a wide soliton with $\xi \gg a_{\rm ho}$, no real solution exists, indicating an absence of minimum in the energy functional and a lack of a stationary state in the vicinity of the potential maximum. On the contrary, for a narrow soliton with $\xi \ll a_{\rm ho}$, the stationary solution exists with its width being roughly the same as that of a free soliton $\xi \approx \xi_f$. The stationary solution exists when the soliton width is smaller than the threshold value $\xi_f/a_{\rm ho} = (0.75/\pi^{1/3})^{0.75} \approx 0.6$, or equivalently, for interaction strengths larger than $|\gamma|N \approx 3.3\sqrt{\hbar^3\omega/m}$. These values provide a reasonable estimate of the threshold value, $\xi_f/a_{\rm ho} \approx 0.45$, shown in Fig. 3.

IV. DYNAMICAL STABILIZATION

The classical pendulum possesses only a single stable position, corresponding to the pendulum stabilized at the bottom, $\theta_1 = 0$, while the equilibrium of the pendulum in the top

position, $\theta_2 = \pi$, is dynamically unstable. Figure 1(c) illustrates that a similar phenomenon occurs in the tilted ring: a weak perturbation, generated by adding a sinusoidal wave on the initial state that shifts the center of mass to $\theta_0 = -3.139$, makes the soliton roll down. Fascinatingly, the inverted position of the pendulum can be stabilized by inducing fast vertical vibrations (along the gravitational field direction) of the pendulum pivot as experimentally shown and mathematically proved by introducing the method of averaging of the fast variables by Pyotr Kapitza in his influential paper [26]. Commonly, the driven pendulum is referred to as a Kapitza pendulum [27]. In contrast, the horizontal vibration moves the equilibrium point to a new position $\theta_2 \neq \pi$ (see Ref. [28], §5, §30). The potential energy of the pivot vibration of frequency $\Omega \gg \omega$ along a generic angle α can be calculated as the work $W = -\mathbf{f} \cdot \mathbf{r}$ done by the two-dimensional (2D) oscillating force $\mathbf{f} = (\cos\alpha, \sin\alpha) m\Omega^2 \ell \sin(\Omega t)$ acting within the ring plane, where $\ell \ll R$ is the characteristic amplitude of the vibration, and $\mathbf{r} = R(\cos\theta, \sin\theta)$ are the ring coordinates. As a result, the total potential energy becomes

$$U(\theta, t) = -m\omega^2 R^2 \left\{ \left[1 - \frac{\Omega^2\ell}{\omega^2 R}\sin(\Omega t)\cos\alpha \right]\cos\theta \right.$$
$$\left. - \frac{\Omega^2\ell}{\omega^2 R}\sin(\Omega t)\sin\alpha \, \sin\theta \right\}. \tag{3}$$

The idea of Kapitza is based on separating processes occurring at slow and fast time scales, i.e., corresponding to low (ω) and high (Ω) frequencies. Then, the slow motion is governed by the effective time-independent potential obtained by time averaging over the fast oscillations,

$$U_{\rm eff}(\theta) = -m\omega^2 R^2 \left\{ \left[\cos\theta - \left(\frac{\beta\cos\alpha\sin\theta}{2} \right)^2 \right] \right.$$
$$\left. - \left(\frac{\beta\sin\alpha\cos\theta}{2} \right)^2 \right\}. \tag{4}$$

where $\beta = \Omega\ell/(\omega R)$ is the ratio between the velocity that characterizes the vibration $\Omega\ell$ and a velocity associated with the unperturbed pendulum ωR. The transition to (classical) stable states takes place at $\beta = \sqrt{2}$. The stability criterion can be stated in terms of energetic quantities, i.e., that the kinetic energy, induced by the driven oscillations, should be large compared to the potential energy above the pivotal point. Figure 4(a) presents characteristic examples illustrating how the effective potential depends on the driving strength β in a deep lattice (specifically, we use $s = 32$). In Fig. 4(a) we focus on the case of vertical driving, i.e., $\alpha = 0$. While for weak driving vibrations ($\beta = 0$ and $\beta = 1$) only a single minimum exists, corresponding to the usual bottom position of the pendulum, $\theta = 0$, for strong driving ($\beta = 2$) the pendulum might flip and a second stable minimum is formed for $\theta = \pm\pi$, corresponding to an inverted pendulum. The case of horizontal driving, $\alpha = \pi/2$, is illustrated in Fig. 4(b). For weak driving oscillations, the usual single minimum is observed. Instead, for sufficiently strong driving, the new (classical) minima appear at $\theta_{1,2} = \pm\pi/3$, while $\theta = 0$ becomes a local maximum.

We have tested the stability of quantum states [the same wave packets described in Fig. 1(c)] subject to the
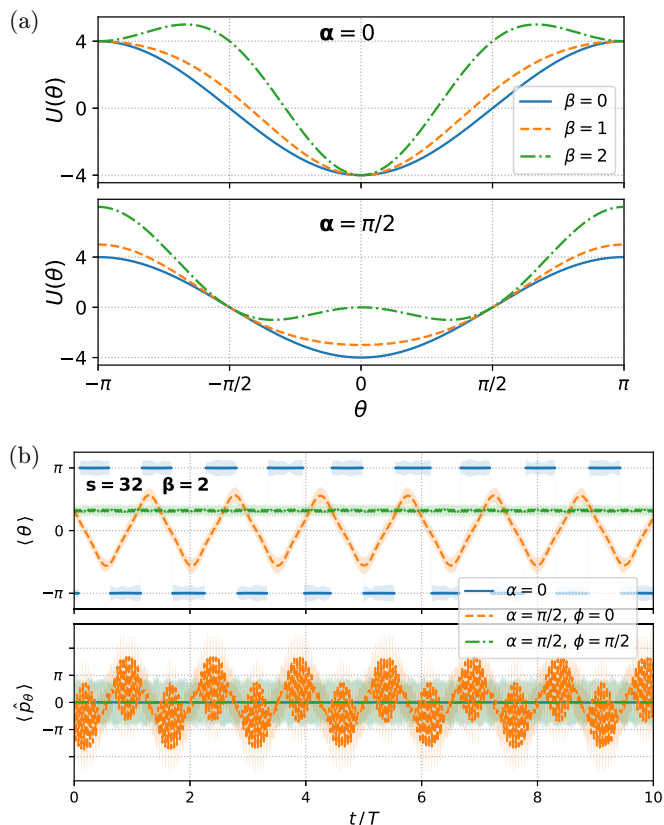
FIG. 4. (a) Effective classical potential in the presence of a fast pivot vibration along the vertical (top panel) and horizontal (bottom panel) directions. (b) Time evolution of wave packets with same parameters as in Fig. 1(c), centered at equilibrium points of the effective potential ($\theta_0 = \pi$ at $\alpha = 0$, solid line, and $\theta_0 = \pi/3$ at $\alpha = \pi/2$, discontinuous lines) and subject to a pivot vibration of amplitude $\ell = 0.1 R$; the phase factor ϕ of the fast vibration imprints a phase profile on the initial state and controls the particle current (negative for $\phi = 0$, dashed line, and zero for $\phi = \pi/2$, dot-dashed line).

time-dependent potential Eq. (3) with vibration amplitude $\ell = 0.1 R$, and centered at the classical equilibrium points of Eq. (4); the outcome is presented in Fig. 4(b). In all considered cases, oscillations of frequency Ω can be observed as fast beating in the evolution of average momentum. For $\alpha = 0$ and $\beta = 2$ (that is, $\Omega = 20 \omega$) the equilibrium point $\theta_2 = \pi$ is stable (solid blue curve), whereas for $\beta = 1$ (not shown) it is not, in agreement with the classical prediction. The situation is not that clear for $\alpha = \pi/2$, since $\beta = 2$ (and $\phi = 0$, see below) does not lead to a static state; instead, the state is induced to tunnel through the local maximum separating the two minima (dashed line), and higher vibrations (for instance, $\beta = 3$, not shown) produce only a partial self-trapping. However, contrary to the classical case, the phase of the vibration is key for the quantum pendulum; introducing a phase factor ϕ in Eq. (3) by the substitution $\Omega t \rightarrow \Omega t + \phi$ has a crucial influence on stability: although $\phi = 0$ does not reproduce the classical result, $\phi = \pi/2$ does (dash-dotted line). The cause resides in the velocity of the initial state (or equivalently its phase) induced by the fast oscillations and controlled by this phase factor, by virtue of which $\phi = \pi/2$ produces a zero

velocity. This mechanism is not qualitatively distinct from the usual phase imprinting technique employed in ultracold-gas experiments [29], and stands as an additional, key stabilization effect in quantum systems, along with the effective classical potential Eq. (4), of Kapitza's procedure.

V. MEASURING GRAVITY

Historically, pendulums were the first devices used to measure gravity, for both absolute and relative measurements, and also the most accurate ones until the second half of the twentieth century, reaching values of $\delta g \approx 10^{-6} g$; afterward, they were replaced by free-fall apparatus [30]. Modern versions of the latter are made of ultracold atoms [31], and have reached top-level performance $\delta g \approx 10^{-9} g$ [32,33]. By means of atomic interferometry, based on a sequence of Raman pulses that split and reunite the falling atomic clouds [34], high-contrast fringes are produced that provide the acceleration of gravity.

Differently, pendulum gravimetry relies on measuring the oscillation period; hence, length, positions, and corresponding times have to be tracked over repeated, small oscillations. In the present quantum pendulum, where dissipation can be ruled out, the atomic cloud can be strongly localized; for instance, an atomic cloud of $N = 2.5 \times 10^4$ particles of ^{7}Li with interaction strength $\gamma = -2\pi \nu \hbar a_0$, where a_0 is the Bohr radius, and harmonic transverse confinement of frequency $\nu = 350$ Hz (similar parameters as in the experiment of Ref. [35], and away from the critical particle number for collapse conditions $N_c \approx 4.5 \times 10^4$, see Refs. [36,37]), has a typical size of $\xi \approx 0.6 \,\mu$m (doubling ν reduces ξ by half and N_c by $\sqrt{2}$). Even within a small ring of radius $R = 12 \,\mu$m, as those of Ref. [38], the relevant parameter $R/\xi = 20$ is large enough to closely reproduce the dynamics of a classical pendulum (with expected relative differences of $\delta \sim 5 \times 10^{-4}$ in the motional periods, see Appendix A). In this case, assuming that shining far-from-resonance light perpendicular to the ring on the atomic cloud does not modify the dynamics, as for classical particles, laser photo-detection could be used to track the motion with expected accuracy of, at least, the order or a few percent (as typically reported in oscillation measurements [39,40]); in-trap nondestructive absorption imaging [35] could also be performed. This uncertainty in measuring the motional period might be reduced by resorting to similar procedures as for the classical reversible pendulums of Kater and Bessel [41]: the measurement of two close but different periods. In the ring, they are associated with different tilts, or equivalently to different lengths $L_j = R/\sin \tau_j$, for $j = 1$, 2, so that gravity is obtained from $g = (2\pi)^2 (L_1^2 - L_2^2)/(L_1 T_1^2 - L_2 T_2^2)$.

A precise determination of the period would also allow one to use the tilted ring for performing sensitive measurements of gravity [33]. By initially preparing the BEC at the energy maximum $\theta = \pi$, where small displacements produce large differences in the period, the presence of a sensible mass at the surface, horizontally located with respect to the ring axis such that δg and g could act orthogonally, would induce an angular displacement $\delta \theta \approx \tan \delta \theta = \delta g/g$. This translates into pendulum periods that can be approximated [see Appendix A, Eq. (A3)] by $T_k(\delta \theta) \approx (2/\pi)(3 \ln 2 - \ln \delta \theta) T$; for

instance, for a void of mass of 100 kg at 1 m apart one obtains $\delta g/g \approx 7 \times 10^{-10}$ and $T_k = 145.5\,T$, while for twice that mass, $\delta g/g \approx 14 \times 10^{-10}$, the period is $T_k = 141.2\,T$.

Since our theoretical analysis is based on a simplified one-dimensional system, it can only point out some sources of uncertainties and estimate their size. Open questions on the role played by extra dimensions, the time taken for the imaging process to become destructive, or how our system could perform in comparison with a free-fall apparatus remain. Alternative potential applications of the quantum pendulum can also be envisaged, e.g., as a sensor based on the Aharonov-Casher effect [42]. These subjects will be addressed elsewhere.

APPENDIX

1. Adiabatic switch of fast vibrations

Instead of suddenly turning on the fast vibrations, as described in the main text, the dynamical stabilization of equilibrium points can also be performed in an adiabatic way. To this end, we have chosen a setup with similar parameters as the ones used in Fig. 4(b) and $\alpha = \pi/2$, but with an initial soliton state of varying amplitude (according to $\tilde{\gamma} = 8$ or 16), centered at the equilibrium point $\theta = 0$ of the nonvibrated system. Subsequently, the amplitude and high frequency of the vibrating potential are adiabatically ramped up, $U(\Omega) = f(t)\,m\Omega^2\,\ell R \sin[f(t)\,\Omega t + \phi] \sin\theta$, where $f(t) = \tanh(0.1\,\omega t)$. Figure 5 shows some characteristic examples for the time evolution of the center of mass in the adiabatic case. As it can be inferred from this figure, the phase factor ϕ still plays a relevant role, and eventually, for $\phi = \pi/2$, the initial state rolls downhill in the effective potential generated by the fast vibration toward one of its energy minima at $\theta = \pi/3$; higher and less regular oscillations around the energy minimum are observed for the more localized soliton (at $\tilde{\gamma} = 16$) due to the higher momentum uncertainty.

2. Classical vs quantum periods of oscillation

For oscillatory motion, the classical equation of the pendulum $\ddot{\theta} + \omega^2 \sin\theta = 0$ has general solutions in terms of elliptic functions $\theta(t) \sim \arcsin[k\,\mathrm{sn}(\omega t, k)]$ (see, for instance, Refs. [43,44]), where $\mathrm{sn}(\omega t, k)$ is the Jacobi elliptic sine function [18] of modulus $k = \sin(\theta_m/2)$, with θ_m being the
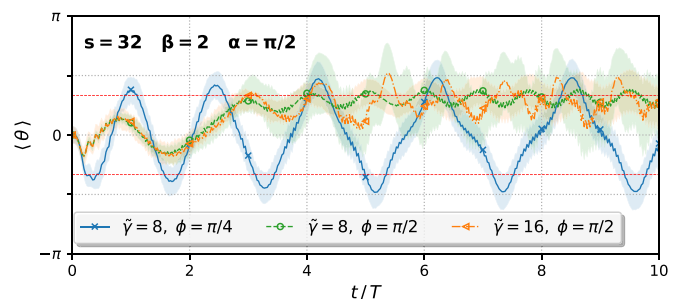

FIG. 5. Time evolution of the center-of-mass position in the case of an adiabatic switch of the fast vibration along the direction $\alpha = \pi/2$. The tilted ring is characterized by a potential depth of $s = 32$. The initial soliton states, featured by the interaction $\tilde{\gamma}$ and situated at $\theta = 0$, move toward the effective energy minima (indicated by horizontal, thin dashed lines) depending on the vibration phase ϕ (see text for additional details).

maximum, turning-point angle. For generic initial conditions, $\theta(0) = \theta_0$ and $\dot{\theta}(0) = \dot{\theta}_0$, the solution reads

$$\theta(t) = \theta_0 + 2\{\arcsin[k\,\mathrm{sn}(\omega t + \varphi_0, k)] \\ - \arcsin[k\,\mathrm{sn}(\varphi_0, k)]\}, \tag{A1}$$

from which it follows that the angular velocity

$$\dot{\theta}(t) = 2k\omega\,\mathrm{cn}(\omega t + \varphi_0, k), \tag{A2}$$

where cn is the Jacobi elliptic cosine function, hence $\varphi_0 = \mathrm{arc\,cn}[\dot{\theta}_0/(2k\,\omega), k]$. The pendulum period is given in terms of the complete elliptic integral of the first kind $K(k)$ [18] as

$$T_k = \frac{K(k)}{\pi/2}\,T, \tag{A3}$$

such that it differs from the period $T = 2\pi/\omega$, achieved in the approximation of small oscillations, by the factor $K(k)/(\pi/2) \in [1, \infty]$ (a monotonically increasing function of k) for $k \in [0, 1]$, that is, for $\theta_m \in [0, \pi]$.

Figure 6 shows a comparison between the classical predictions of Eqs. (A1)–(A3) and the mean values of the motion of free-soliton wave packets (2) in a tilted ring. As one could expect, the period predicted by Eq. (A3), $T_k = 1.0732\,T$, is better approached at higher interactions $\tilde{\gamma} = 16$. By averaging over 25 periods of oscillation in order to minimize the uncertainty in the measured times, we obtain the differences $\delta(\tilde{\gamma}) = [T_k(\tilde{\gamma}) - T_k]/T_k$ to be $\delta(\tilde{\gamma} = 16) = 3.36 \times 10^{-3}$ and $\delta(\tilde{\gamma} = 8) = 1.23 \times 10^{-2}$; a slight reduction is found for initial conditions closer to equilibrium positions, for instance, $\delta(\tilde{\gamma} = 16) = 3.14 \times 10^{-3}$ for $\theta_0 = 3\pi/4$.

These differences can be understood by considering the Ehrenfest equation $d^2\langle\theta\rangle/dt^2 + \omega^2\langle\sin\theta\rangle = 0$, which exactly matches the functional form of the classical equation, as $d^2\langle\theta\rangle/dt^2 + \omega^2 \sin\langle\theta\rangle = 0$, only when the density profile of the soliton wave function becomes a Dirac delta function $|\psi_{BS}(\theta - \theta_0)|^2 \to \delta(\theta - \theta_0)$; otherwise, the difference between both equations can be written as the power series

$$\Delta = \langle\sin\theta\rangle - \sin\langle\theta\rangle = \sum_{\substack{n \geq 3 \\ n\,\text{odd}}}^{n \geq 3} \frac{(-1)^{\frac{n-1}{2}}}{n!}(\langle\theta^n\rangle - \langle\theta\rangle^n). \tag{A4}$$
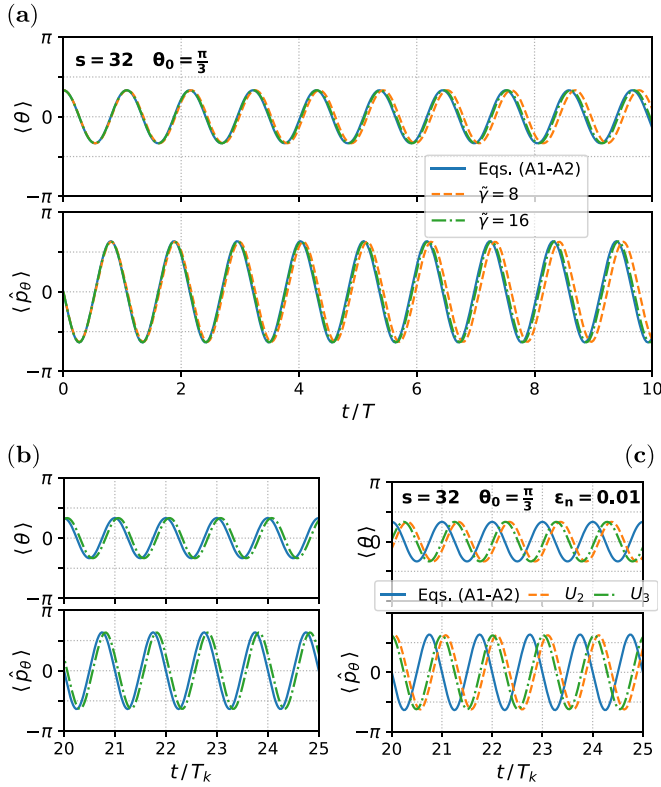
FIG. 6. Comparison between the motions of the classical pendulum and the soliton as given by Eq. (2). Time evolution of the center of mass $\langle\theta\rangle$ and the angular momentum $\langle\hat{p}_\theta\rangle$ is shown in a tilted ring characterized by $s = 32$ using initial conditions $\theta_0 = \pi/3$ and $\dot{\theta}_0 = 0$. Different interactions, parametrized by $\tilde{\gamma} = 2R/\xi$, translate into different wave-packet widths ξ. (a) Short-time evolution for $\tilde{\gamma} = 8$ and $\tilde{\gamma} = 16$. (b) Long-time evolution for $\tilde{\gamma} = 16$. (c) Time evolution in a perturbed ring potential $U_n(\theta) = -m\omega^2 R^2[\cos\theta - \epsilon_n \cos(n\theta)]$, with $n = 2, 3$.

For a free soliton state Eq. (2) of width ξ and moving center $\theta_0(t)$, the above series can be approximated, for large ratios $(R/\xi = \tilde{\gamma}/2) \gg 1$, up to second order, by

$$\Delta(\tilde{\gamma}) \approx -\frac{\pi^2}{6\tilde{\gamma}^2}\sin\langle\theta\rangle, \qquad (A5)$$

where we made use of $\langle\theta\rangle = \theta_0(t)$. This result amounts to having an effective classical equation with a slightly reduced

angular frequency $\omega(\tilde{\gamma}) = \omega\sqrt{1 - \pi^2/(6\tilde{\gamma}^2)}$, or, equivalently, a slightly increased small-oscillation period

$$T(\tilde{\gamma}) \approx \left(1 + \frac{\pi^2}{12\tilde{\gamma}^2}\right)T. \qquad (A6)$$

Evaluated at the values $\tilde{\gamma} = 8$ and 16, used in Fig. 6, this estimate produces $\delta(\tilde{\gamma} = 8) = 1.31 \times 10^{-2}$, and $\delta(\tilde{\gamma} = 16) = 3.23 \times 10^{-3}$, in good agreement with the measured results previously reported.

Ring roundness

Small azimuthal variations in the ring potential can also give rise to alterations in the period of the motion. In order to estimate the effect of such variation, we have introduced a perturbed potential $U_n(\theta) = -m\omega^2 R^2[\cos\theta - \epsilon_n \cos(n\theta)]$, with a small integer $n > 1$, and $\epsilon_n \ll 1$. It translates into an extra force term $F_n(\theta) = \epsilon_n m\omega^2 R n\langle\sin(n\theta)\rangle$ in the corresponding Ehrenfest equation that can also be calculated as a power series up to second order in $\tilde{\gamma}^{-1}$ as

$$F_n(\tilde{\gamma}) \approx \epsilon_n m\omega^2 R n\left(1 - \frac{n^2\pi^2}{6\tilde{\gamma}^2}\right)\sin\langle n\theta\rangle. \qquad (A7)$$

In the limit of small oscillations, a perturbed single frequency, $\omega_n(\tilde{\gamma}) = \omega\sqrt{1 - \epsilon_n[n^2 - n^4\pi^2/(6\tilde{\gamma}^2)]}$, can be obtained; for instance, by setting $n = 2$, 3, and $\epsilon_n = 0.01$, this estimate provides us with the order of magnitude of the perturbed period observed in our numerical results, as shown in Fig. 6(c), where we have measured $\delta_2(\tilde{\gamma} = 16) = 1.57 \times 10^{-2}$ and $\delta_3(\tilde{\gamma} = 16) = 1.16 \times 10^{-2}$. From the reported data, it becomes clear that the azimuthal variations of the ring potential can introduce a significant source of uncertainty in the measured observables, at least in the search for high-precision measurements (see, e.g., Ref. [45]); in this regard, time-averaging optical ring potentials [46] could be useful to achieve improved trap smoothness.

3. Numerical solutions

Gross-Pitaevskii Eq. (1) has been numerically solved through FFT techniques for the spatial discretization, and standard, high-order (typically 5–9) time integrators of Julia programming language. For time-independent solutions, both imaginary time evolution, for the ground state, and Newton method, for excited states as those presented in Fig. 3, have been used.

[1] M. Van Camp, O. de Viron, A. Watlet, B. Meurers, O. Francis, and C. Caudron, Geophysics from terrestrial time-variable gravity measurements, Rev. Geophys. **55**, 938 (2017).

[2] C. Ryu, M. F. Andersen, P. Cladé, V. Natarajan, K. Helmerson, and W. D. Phillips, Observation of persistent flow of a Bose-Einstein condensate in a toroidal trap, Phys. Rev. Lett. **99**, 260401 (2007).

[3] W. H. Heathcote, E. Nugent, B. T. Sheard, and C. J. Foot, A ring trap for ultracold atoms in an RF-dressed state, New J. Phys. **10**, 043012 (2008).

[4] A. Ramanathan, K. C. Wright, S. R. Muniz, M. Zelan, W. T. Hill, C. J. Lobb, K. Helmerson, W. D. Phillips, and G. K. Campbell, Superflow in a toroidal Bose-Einstein condensate: An atom circuit with a tunable weak link, Phys. Rev. Lett. **106**, 130401 (2011).

[5] S. Moulder, S. Beattie, R. P. Smith, N. Tammuz, and Z. Hadzibabic, Quantized supercurrent decay in an annular Bose-Einstein condensate, Phys. Rev. A **86**, 013629 (2012).

[6] S. Pandey, H. Mas, G. Drougakis, P. Thekkeppatt, V. Bolpasi, G. Vasilakis, K. Poulios, and W. von Klitzing, Hypersonic

Bose-Einstein condensates in accelerator rings, Nature (London) **570**, 205 (2019).

[7] A. Smerzi, S. Fantoni, S. Giovanazzi, and S. R. Shenoy, Quantum coherent atomic tunneling between two trapped Bose-Einstein condensates, Phys. Rev. Lett. **79**, 4950 (1997).

[8] O. Fialko, B. Opanchuk, A. I. Sidorov, P. D. Drummond, and J. Brand, Fate of the false vacuum: Towards realization with ultra-cold atoms, Europhys. Lett. **110**, 56001 (2015).

[9] M. Pigneur and J. Schmiedmayer, Analytical pendulum model for a bosonic Josephson junction, Phys. Rev. A **98**, 063632 (2018).

[10] O. Fialko, M.-C. Delattre, J. Brand, and A. R. Kolovsky, Nucleation in finite topological systems during continuous metastable quantum phase transitions, Phys. Rev. Lett. **108**, 250402 (2012).

[11] I. Gilary, N. Moiseyev, S. Rahav, and S. Fishman, Trapping of particles by lasers: The quantum Kapitza pendulum, J. Phys. A: Math. Gen. **36**, L409 (2003).

[12] J. Jiang, E. Bernhart, M. Röhrle, J. Benary, M. Beck, C. Baals, and H. Ott, Kapitza trap for ultracold atoms, Phys. Rev. Lett. **131**, 033401 (2023).

[13] W. He and C.-Y. Liu, Oscillatory states of quantum Kapitza pendulum, Ann. Phys. **449**, 169218 (2023).

[14] F. Kh. Abdullaev and R. Galimzyanov, The dynamics of bright matter wave solitons in a quasi one-dimensional Bose-Einstein condensate with a rapidly varying trap, J. Phys. B: At. Mol. Opt. Phys. **36**, 1099 (2003).

[15] C. J. Richards, T. J. Smart, P. H. Jones, and D. Cubero, A microscopic Kapitza pendulum, Sci. Rep. **8**, 13107 (2018).

[16] E. U. Condon, The physical pendulum in quantum mechanics, Phys. Rev. **31**, 891 (1928).

[17] M. A. Doncheski and R. W. Robinett, Wave packet revivals and the energy eigenvalue spectrum of the quantum pendulum, Ann. Phys. **308**, 578 (2003).

[18] DLMF, NIST Digital Library of Mathematical Functions, http://dlmf.nist.gov/, Release 1.0.28 of 2020-09-15 (2023).

[19] A. Muñoz Mateo, V. Delgado, M. Guilleumas, R. Mayol, and J. Brand, Nonlinear waves of Bose-Einstein condensates in rotating ring-lattice potentials, Phys. Rev. A **99**, 023630 (2019).

[20] I. Bloch, J. Dalibard, and W. Zwerger, Many-body physics with ultracold gases, Rev. Mod. Phys. **80**, 885 (2008).

[21] O. Morsch and M. Oberthaler, Dynamics of Bose-Einstein condensates in optical lattices, Rev. Mod. Phys. **78**, 179 (2006).

[22] C. Kittel and P. McEuen, *Introduction to Solid State Physics* (Wiley, New York, 2018).

[23] M. Olshanii, Atomic scattering in the presence of an external confinement and a gas of impenetrable bosons, Phys. Rev. Lett. **81**, 938 (1998).

[24] P. J. Y. Louis, E. A. Ostrovskaya, C. M. Savage, and Y. S. Kivshar, Bose-Einstein condensates in optical lattices: Band-gap structure and solitons, Phys. Rev. A **67**, 013602 (2003).

[25] L. P. Pitaevskii and S. Stringari, *Bose-Einstein Condensation*, International Series of Monographs on Physics (Oxford University, New York, 2003).

[26] P. L. Kapitza, Dynamic stability of a pendulum with an oscillating point of suspension, JETP **21**, 588 (1951).

[27] G. E. Astrakharchik and N. A. Astrakharchik, Numerical study of Kapitza pendulum, arXiv:1103.5981.

[28] L. D. Landau and E. M. Lifshitz, *Mechanics*, 3rd ed. (Elsevier, Oxford, 2000).

[29] Ł. Dobrek, M. Gajda, M. Lewenstein, K. Sengstock, G. Birkl, and W. Ertmer, Optical generation of vortices in trapped Bose-Einstein condensates, Phys. Rev. A **60**, R3381 (1999).

[30] M. A. Zumberge, Gravity measurements, absolute, *in Encyclopedia of Solid Earth Geophysics*, edited by H. K. Gupta (Springer, Cham, 2021), p. 633.

[31] J. E. Debs, P. A. Altin, T. H. Barter, D. Döring, G. R. Dennis, G. McDonald, R. P. Anderson, J. D. Close, and N. P. Robins, Cold-atom gravimetry with a Bose-Einstein condensate, Phys. Rev. A **84**, 033610 (2011).

[32] V. Ménoret, P. Vermeulen, N. Le Moigne, S. Bonvalot, P. Bouyer, A. Landragin, and B. Desruelle, Gravity measurements below 10^{-9} g with a transportable absolute quantum gravimeter, Sci. Rep. **8**, 12300 (2018).

[33] B. Stray *et al.*, Quantum sensing for gravity cartography, Nature (London) **602**, 590 (2022).

[34] M. Kasevich and S. Chu, Atomic interferometry using stimulated Raman transitions, Phys. Rev. Lett. **67**, 181 (1991).

[35] J. H. V. Nguyen, D. Luo, and R. G. Hulet, Formation of matter-wave soliton trains by modulational instability, Science **356**, 422 (2017).

[36] V. M. Pérez-García, H. Michinel, J. I. Cirac, M. Lewenstein, and P. Zoller, Dynamics of Bose-Einstein condensates: Variational solutions of the Gross-Pitaevskii equations, Phys. Rev. A **56**, 1424 (1997).

[37] V. M. Pérez-García, H. Michinel, and H. Herrero, Bose-Einstein solitons in highly asymmetric traps, Phys. Rev. A **57**, 3837 (1998).

[38] S. Beattie, S. Moulder, R. J. Fletcher, and Z. Hadzibabic, Persistent currents in spinor condensates, Phys. Rev. Lett. **110**, 025301 (2013).

[39] B. Fang, G. Carleo, A. Johnson, and I. Bouchoule, Quench-induced breathing mode of one-dimensional Bose gases, Phys. Rev. Lett. **113**, 035301 (2014).

[40] B. Huang, I. Fritsche, R. S. Lous, C. Baroni, J. T. M. Walraven, E. Kirilov, and R. Grimm, Breathing mode of a Bose-Einstein condensate repulsively interacting with a fermionic reservoir, Phys. Rev. A **99**, 041602(R) (2019).

[41] J. H. Poynting and J. J. Thomson, *A Textbook of Physics* (Griffin, London, 1908).

[42] This potential application has been suggested to us by an anonymous referee.

[43] K. R. Symon, *Mechanics*, Addison-Wesley Series in Physics (Addison-Wesley Publishing, Reading, 1971).

[44] M. Tabor, *Chaos and Integrability in Nonlinear Dynamics: An Introduction* (Wiley, New York, 1989).

[45] M. de Goër de Herve, Y. Guo, C. De Rossi, A. Kumar, T. Badr, R. Dubessy, L. Longchambon, and H. Perrin, A versatile ring trap for quantum gases, J. Phys. B: At. Mol. Opt. Phys. **54**, 125302 (2021).

[46] T. A. Bell, J. A. P. Glidden, L. Humbert, M. W. J. Bromley, S. A. Haine, M. J. Davis, T. W. Neely, M. A. Baker, and H. Rubinsztein-Dunlop, Bose-Einstein condensation in large time-averaged optical ring potentials, New J. Phys. **18**, 035003 (2016).